

Bayesian inference of multimessenger astrophysical data: Joint and coherent inference of gravitational waves and kilonovae

Matteo Breschi^{1,2,3}, Rossella Gamba^{1,4,5}, Gregorio Carullo^{1,6}, Daniel Godzieba⁴,
Sebastiano Bernuzzi¹, Albino Perego^{7,8}, and David Radice^{4,9,10} *

¹ Theoretisch-Physikalisches Institut, Friedrich-Schiller-Universität Jena, Fröbelstieg 1, 07743 Jena, Germany

² Scuola Internazionale Superiore di Studi Avanzati (SISSA), via Bonomea 265, 34136 Trieste, Italy

³ Istituto Nazionale di Fisica Nucleare (INFN), Sezione di Trieste, via Valerio 2, 34127 Trieste, Italy

⁴ Institute for Gravitation & the Cosmos, The Pennsylvania State University, University Park PA 16802, USA

⁵ Department of Physics, University of California, Berkeley, CA 94720, USA

⁶ Niels Bohr International Academy, Niels Bohr Institute, Blegdamsvej 17, 2100 Copenhagen, Denmark

⁷ Dipartimento di Fisica, Università di Trento, Via Sommarive 14, 38123 Trento, Italy

⁸ INFN-TIFPA, Trento Institute for Fundamental Physics and Applications, via Sommarive 14, I-38123 Trento, Italy

⁹ Department of Physics, The Pennsylvania State University, University Park PA 16802, USA

¹⁰ Department of Astronomy & Astrophysics, The Pennsylvania State University, University Park PA 16802, USA

January 9, 2024

ABSTRACT

Context. Multimessenger observations of binary neutron star mergers can provide information on the neutron star’s equation of state (EOS) above nuclear saturation density by directly constraining the mass-radius diagram.

Aims. We present a Bayesian framework for joint and coherent analyses of multimessenger binary neutron star signals. As a first application, we analyze the gravitational-wave GW170817 and the kilonova AT2017gfo data. These results are then combined with the most recent X-ray pulsars analyses of PSR J0030+0451 and PSR J0740+6620 to obtain EOS constraints.

Methods. We extend the *bajes* infrastructure with a joint likelihood for multiple datasets, support for various semi-analytical kilonova models and numerical-relativity (NR) informed relations for the mass ejecta, as well as a technique to include and marginalize over modeling uncertainties. The analysis of GW170817 uses the *TEOBResumS* effective-one-body waveform template to model the gravitational-wave signal. The analysis of AT2017gfo uses a baseline multi-component spherically symmetric model for the kilonova (kN) light curves. Various constraints on the mass-radius diagram and neutron star properties are then obtained by resampling over a set of ten million parametrized EOS built under minimal assumptions.

Results. We find that a joint and coherent approach improves the inference of the extrinsic parameters (distance) and, among the intrinsic parameters, the mass ratio. The inclusion of NR informed relations strongly improves over the case of using an agnostic prior on the intrinsic parameters. Comparing Bayes factors, we find that the two observations are better explained by the common source hypothesis only by assuming NR-informed relations. These relations break some of the degeneracies in the employed kN models. The EOS inference folding-in PSR J0952-0607 minimum-maximum mass, PSR J0030+0451 and PSR J0740+6620 data constrains, among other quantities, the neutron star radius to $R_{1.4}^{\text{TOV}} = 12.30^{+0.81}_{-0.56}$ km ($R_{1.4}^{\text{TOV}} = 13.20^{+0.91}_{-0.90}$ km) and the maximum mass to $M_{\text{max}}^{\text{TOV}} = 2.28^{+0.25}_{-0.17} M_{\odot}$ ($M_{\text{max}}^{\text{TOV}} = 2.32^{+0.30}_{-0.19} M_{\odot}$) where the ST+PDT (PDT-U) analysis for PSR J0030+0451 is employed. Hence, the systematics on PSR J0030+0451 data reduction currently dominate the mass-radius diagram constraints.

Conclusions. We conclude that *bajes* delivers robust analyses in-line with other state-of-art results in the literature. Strong EOS constraints are provided by pulsars observations, albeit with large systematics in some cases. Current gravitational-wave constraints are compatible with pulsars constraints and can further improve the latter.

Key words. Equation of state, Gravitational waves, Stars: neutron, pulsars: general, Methods: data analysis

1. Introduction

The observation of the gravitational wave (GW) signal GW170817 from a binary neutron star merger and its electromagnetic counterparts from the merger aftermath opened new prospects to constrain the nature of neutron star (NS) matter (Abbott et al. 2017b,a, 2019b). GWs from the late-inspiral-to-merger frequencies carry the imprint of short-range tidal interactions between the two NSs (Damour & Deruelle 1986; Damour & Nagar 2010). The measurement of tidal polarizability parameters, in particular the reduced tidal parameter $\tilde{\Lambda}$ appearing in the leading-order term of the GW phase (Damour et al. 2012;

Favata 2014), constrains the nuclear equation of state (EOS) (Abbott et al. 2018; De et al. 2018). For GW170817, various analyses indicate posterior distributions peaking in the interval $100 \lesssim \tilde{\Lambda} \lesssim 800$, that can be mapped on a NS radius ¹ constraint of $R_{1.4}^{\text{TOV}} = 12.5^{+1.1}_{-1.8}$ km at 90% credibility (Gamba et al. 2021b).

Electromagnetic counterparts can complement such constraints by delivering information on the merger remnant. For example, the high-energy emission from a jet-like source of GRB170817 (Abbott et al. 2017a; Savchenko et al. 2017) is as-

¹ As common in the literature, we call NS radius the radius $R_{1.4}^{\text{TOV}}$ of nonrotating, cold beta-equilibrated NS of fiducial gravitational mass $1.4M_{\odot}$. These general-relativistic equilibrium configurations are calculated by solving the Tolmann-Oppenheimer-Volkhoff equations.

* Alfred P. Sloan Fellow

sociated to the presence of a remnant black hole and can thus constrain the maximum NS mass (Margalit & Metzger 2017; Shibata et al. 2017) (see also Margalit et al. (2022) for a revision of the first calculation.) The interpretation of the kilonova (kN) AT2017gfo (Coulter et al. 2017; Chornock et al. 2017; Nicholl et al. 2017; Cowperthwaite et al. 2017; Pian et al. 2017; Smartt et al. 2017; Tanvir et al. 2017; Tanaka et al. 2017; Valenti et al. 2017) requires different mass ejecta components *e.g.* (Villar et al. 2017; Perego et al. 2017b; Breschi et al. 2021b), thus excluding a prompt black hole formation (Margalit & Metzger 2017; Bauswein et al. 2017). Further, the necessity of including a massive disc wind to interpret the light curves implies a lower limit (as opposite to the GW upper limit) on the reduced tidal parameter (Radice et al. 2018c,b).

The rigorous analysis of multi-messenger astrophysics (MMA) data requires a Bayesian approach. Bayesian inference of GW170817 and related counterparts with application to the NS EOS has been performed by various authors, *e.g.* (Radice & Dai 2019; Coughlin et al. 2019; Capano et al. 2020; Jiang et al. 2020; Essick et al. 2020; Dietrich et al. 2020; Al-Mamun et al. 2021; Nicholl et al. 2021; Breschi et al. 2021b; Raaijmakers et al. 2021a; Ayriyan et al. 2021; Huth et al. 2022; Pang et al. 2022; Brandes et al. 2023; Fan et al. 2023). These analyses provide bounds or posterior distributions on fiducial NS masses, radii, quadrupolar tidal polarizability parameters, as well as on pressure (or energy density), sound speed at fiducial points or even nuclear parameters (given a EOS parametrization). Some results about the NS radius are collected in Fig. 12 of Breschi et al. (2021b), indicating a substantial agreement among various analyses, with $R_{1.4}^{\text{TOV}} \approx 12$ km and 90% credible intervals at the kilometer level, depending on the specific assumptions. Note that, in several cases, these analyses incorporate assumption on the EOS (Jiang et al. 2020; Greif et al. 2020; Huang et al. 2023; Fan et al. 2023) including available experimental nuclear data *e.g.* (Danielewicz et al. 2002; Hebeler et al. 2013; Le Fèvre et al. 2016; Russotto et al. 2016).

Despite the potential of MMA observations of NS mergers, data from GW170817 and counterparts alone do not significantly constrain the nuclear physics of dense NS matter yet, *e.g.* (Al-Mamun et al. 2021; Greif et al. 2020). The lower bound to the maximum NS mass $M_{\text{max}}^{\text{TOV}}$ (“minimum-maximum mass”), provided by pulsars observations (Demorest et al. 2010; Miller et al. 2019; Romani et al. 2022; Godzieba et al. 2021), matter. These data rule out a large number of EOS models, including some containing hyperons or deconfined quark matter Hebeler et al. (2013) (though the latter are still viable, see *e.g.* Annala et al. (2020)). The most massive NS identified so far is PSR J0952–0607, a millisecond pulsar in a binary system, with $M_{\text{J0740+6620}} = 2.35 \pm 0.17 M_{\odot}$ Romani et al. (2022). Recent X-ray observations of isolated pulsars have been performed by NICER and XMM-Newton (Miller et al. 2019; Riley et al. 2019; Miller et al. 2021; Riley et al. 2021). These observations targeted PSR J0030+0451 (Miller et al. 2019; Riley et al. 2021; Raaijmakers et al. 2019) and PSR J0740+6620 (Miller et al. 2021). The former NS has a best radius and mass estimates of $R_{\text{J0030+0451}} = 12.71^{+1.14}_{-1.19}$ km and $M_{\text{J0030+0451}} = 1.24^{+0.15}_{-0.16} M_{\odot}$ (68% credibility) (Miller et al. 2019) (see also (Riley et al. 2019)). The latter NS has the second-heaviest reliably determined mass to-date $M_{\text{J0740+6620}} = 2.08 \pm 0.07 M_{\odot}$ with a radius of $R_{\text{J0740+6620}} = 13.7^{+2.6}_{-1.5}$ km (68% credibility) (Miller et al. 2021). Overall, these data constrain the mass and radius of the NS at the $\lesssim 5\%$ level. Several MMA analyses have combined binary neutron star merger with pulsar data, *i.e.* used data from multiple sources, to improve astrophysical EOS constraints (Jiang et al.

2020; Essick et al. 2020; Dietrich et al. 2020; Al-Mamun et al. 2021; Nicholl et al. 2021; Breschi et al. 2021b; Raaijmakers et al. 2021a; Ayriyan et al. 2021; Brandes et al. 2023; Fan et al. 2023). Recently, Vinciguerra et al. (2023) re-analysed PSR J0030+0451 with an improved pipeline, finding updated measurements of both the mass and radius of the pulsar depending on the employed hot-spots model: $(M, R)_{\text{J0030+0451}} = (1.4^{+0.13}_{-0.12}, 11.71^{+0.88}_{-0.83})$ (ST+PDT) or $(M, R)_{\text{J0030+0451}} = (1.7^{+0.18}_{-0.19}, 14.44^{+0.88}_{-1.05})$ (PDT-U).

Methodologically, MMA analyses share several common features. We comment on three of such common elements, that are later incorporated in our work. (i) The use of phenomenological relations from numerical-relativity (NR) simulations, incorporating remnant constraints into GW analysis. Accurate simulation results are, for example, available to build equal-mass prompt collapse models, *e.g.* (Hotokezaka et al. 2011; Bauswein et al. 2013a; Agathos et al. 2020; Kashyap et al. 2022; Perego et al. 2022). Simple models describing kinematic quantities of dynamical ejecta (Dietrich & Ujevic 2017; Radice et al. 2018b; Krüger & Foucart 2020; Nedora et al. 2022) and remnant disc masses Radice et al. (2018b); Krüger & Foucart (2020); Nedora et al. (2022) in terms of the binary properties are also available. However, such relationships are subject to significant systematics, depending on the physics input of the simulations (Nedora et al. 2022). (ii) The assumption of a EOS catalog in order to map the posteriors of the inferred parameters into other set of parameters. The typical sample size of this catalog ranges from a few tens to a few thousands EOS curves. These EOS sets may be constructed from model-agnostic piecewise polytropic representations *e.g.* (Jiang et al. 2020; Raaijmakers et al. 2021a) or assuming nuclear theories, such as like chiral effective theory and perturbative quantum chromodynamics in their regime of validity *e.g.* (Essick et al. 2020; Fan et al. 2023). This implies different prior assumptions between different analyses, and makes a direct comparison of the results problematic. However, it should be noted that the vast majority of the employed EOS sets include constraints coming from massive pulsars (Antoniadis et al. 2013; Cromartie et al. 2019), sharing part of their prior information (additional details are provided below). (iii) MMA analyses are often performed independently for each dataset, combining in postprocessing the posterior distributions for the relevant parameters. While this approach is justified for data coming from independent sources, the analysis of different data from a single source may benefit from joint coherent analyses, especially in the case of large correlations between parameters describing the different dataset and in the presence of modelling systematics. The *single-source–multiple-data* scenario can be rigorously handled within the Bayesian framework by joinining the single messenger likelihoods and performing a combined sampling of the full posterior probability distribution *e.g.* (Biscoveanu et al. 2020; Pang et al. 2022); we refer to these analyses as *joint and coherent*.

In this work, we present a new framework for joint-and-coherent MMA Bayesian analyses. We apply our framework to the case of GW170817 and AT2017gfo and provide updated constraints on the NS EOS. The structure and summary of the paper is as follows.

Sec. 2 describes the methods employed in our analysis, and presents the extension of the *bajes* pipeline (Breschi et al. 2021b) to MMA data.

Sec. 3 describes the results of applying *bajes-MMA* on GW170817 and AT2017gfo data. We employ a state-of-art effective-one-body (EOB) template and a spherically symmetric multi-component semi-analytical kN model. We compare single messenger analyses to joint & coherent analyses used either an

agnostic prior on intrinsic parameters or a NR-informed prior on intrinsic parameters.

Sec. 4 discusses EOS constraints from our new analyses. We use a set of ~ 10 million parameterized EOS built under minimal assumptions, namely assuming general relativity, causality and a minimum-maximum mass of $2.09M_\odot$ Romani et al. (2022). We combine GW170817+At2017gfo data with independent pulsar data and include, for the first time, the recent re-analysis of Vinciguerra et al. (2023).

Conclusions and an Appendix on new fitting formulas close the paper.

2. Methods

Our analyses are based on Bayesian probability, which delivers information on the source parameters in terms of their posterior probability distributions, an accurate characterization of the correlations among parameters and the possibility of ranking different hypotheses to explain the data (e.g. Jeffreys 1939). Given the observed data \mathbf{d} and a set of parameters θ that characterize a model for the data (hypothesis H), the information on the parameters is encoded in the posterior distribution $p(\theta|\mathbf{d}, H)$. Using Bayes theorem, $p(\theta|\mathbf{d}, H)$ can be computed as the product of the likelihood function $p(\mathbf{d}|\theta, H)$ and the prior distribution of the model parameters $p(\theta|H)$. The evidence $p(\mathbf{d}|H)$ is instead employed in the context of model selection in order to discriminate different models. Given two different hypotheses, say H_A and H_B , the Bayes' factor (BF)

$$\mathcal{B}_B^A = \frac{p(\mathbf{d}|H_A)}{p(\mathbf{d}|H_B)}, \quad (1)$$

encodes the support of the data in favoring hypothesis A against hypothesis B (within the assumption of uniform prior on $H_{A,B}$)².

For multimessenger astrophysics data, the high-dimensional parameters' posterior distribution can have non-trivial correlations and multimodalities. Numerical stochastic methods are the essential tools in order to perform parameter estimation (PE). We employ the *bajes* pipeline (Breschi et al. 2021b) together with the nested sampling algorithm (e.g. Skilling 2006; Feroz et al. 2009), implemented in the *DYNesty* nested sampler (Speagle 2020). All the PE runs presented here are performed with 5000 live points and using *bajes* parallel capabilities. In the following, we describe the data, the likelihood functions, the models and the prior utilized for the analyses.

2.1. Gravitational waves inference

The time-series recorded by the ground-based interferometers LIGO and Virgo can be modeled as the sum of a noise contribution $n(t)$ and a GW transient $h(t)$, i.e. $d(t) = h(t) + n(t)$. The signal observed by the interferometers is computed from the GW polarizations $h_{+,\times}$ as

$$h(t) = F_+(\alpha, \delta, \psi) h_+(t) + F_\times(\alpha, \delta, \psi) h_\times(t), \quad (2)$$

where $F_{+,\times}$ are the antenna pattern functions of the employed detector (see, e.g. Anderson et al. 2001) that are functions of the source location $\{\alpha, \delta\}$ and the polarization angle ψ . We

² In order to lighten the notation, the explicit dependency of a statistical quantity $p(x|H)$ on the corresponding underlying hypotheses H is made implicit when not necessary, i.e. $p(x|H) \mapsto p(x)$.

analyze the GW data segment $d(t)$ from the Gravitational-Wave Open Science Center (GWOSC) centered around GPS time 1187008857 with duration $T = 128$ s and sampling rate 4096 Hz (Abbott et al. 2017b, 2019a).

We analyze the GW signal $h(t)$ assuming a quasi-circular BNS merger and employing the effective-one-body (EOB) model TEOBRESUMS (Bernuzzi et al. 2015; Nagar et al. 2018; Akcay et al. 2019; Nagar et al. 2020; Gamba et al. 2021a) with tidal and non-precessing spins interactions. We include the dominant quadrupolar (2,2) mode of the radiation in the waveform construction, and use for efficiency the post-adiabatic method (Nagar & Rettegno 2019) for the EOB dynamics and the stationary-phase approximation for frequency domain waveforms (Gamba et al. 2021a). We stress that this EOB model is faithful to NR within its error bands, and that systematic errors due to modeling choices are sub-dominant with respect to statistical uncertainties for the GW analysis (Abbott et al. 2019c; Gamba et al. 2021b).

The GW template $h(t; \theta_{\text{gw}})$ is parameterized by 15 degrees of freedom,

$$\theta_{\text{gw}} = \{m_1, m_2, \chi_1, \chi_2, \Lambda_1, \Lambda_2, D_L^{\text{gw}}, \iota^{\text{gw}}, \psi, t_{\text{mrg}}^{\text{gw}}, \phi_{\text{mrg}}\}, \quad (3)$$

where $m_{1,2}$ are the component masses, $\chi_{1,2}$ are the components of dimensionless spins aligned to the orbital angular momentum, $\Lambda_{1,2}$ are the dimensionless quadrupolar tidal polarizabilities, D_L^{gw} is the luminosity distance, ι^{gw} is the inclination angle between the line of sight and the total angular momentum of the system, and $t_{\text{mrg}}^{\text{gw}}$ and ϕ_{mrg} are respectively the time and the phase at merger. The GW superscript means that these parameters are the one associated with the GW signal, and the need for this distinction is made clear below. For simplicity, the sky position is fixed to the location of the optical counterpart (Abbott et al. 2017c), i.e. right ascension 13h 09m 48s and declination -23.3814 degrees. Note that we assume $m_1 \geq m_2$ and introduce the total binary mass $M = m_1 + m_2$ and the mass ratio $q = m_1/m_2$. The leading order tidal contribution in the GW template is parameterized by the reduced tidal polarizability $\tilde{\Lambda}$ defined as (Damour & Nagar 2009; Favata 2014)

$$\tilde{\Lambda} = \frac{16}{13} \left[\frac{(m_1 + 12m_2)m_1^4}{M^5} \Lambda_1 + (1 \leftrightarrow 2) \right]. \quad (4)$$

Data analyses of GW transients relies on the assumptions of stationarity and Gaussianity of the noise in each detector, from which we can write a Gaussian likelihood function in the Fourier domain as

$$\log p(\mathbf{d}_{\text{gw}}|\theta_{\text{gw}}) = -\frac{2}{T} \sum_i \frac{|\tilde{d}(f_i) - \tilde{h}(f_i)|^2}{S_n(f_i)} + \log \left[\frac{\pi T}{2} S_n(f_i) \right], \quad (5)$$

where $\tilde{h}(f)$ is the Fourier transform of $h(t)$ (and analogously for $\tilde{d}(f)$) while $S_n(f)$ is the power spectral density (PSD) of the noise segment (Abbott et al. 2019a). The sum in Eq. (5) is on the sampled frequencies and evaluated over the frequency interval [23 Hz, 2 kHz]. Note that Gamba et al. (2021b) showed that GW analyses up to 2 kHz are affected by larger systematics than those at 1 kHz on the tidal sector, with the latter choice being more robust but also more conservative. Since systematics effects are generically smaller than other systematic effects discussed in this papers, we use here the more commonly used 2 kHz cut off. Under the assumption that noise fluctuations recorded in different detectors are not correlated, the likelihood of the detector network is computed as the product of the individual likelihoods. We include spectral calibration envelopes

with 10 logarithmically-spaced nodes for each detector (see, e.g. Vitale et al. 2012).

The priors are the same as those discussed in Breschi et al. (2021b), with mass ratio bounded to $q \leq 3$, isotropically-distributed spins $\chi_{1,2}$ constrained to $|\chi_{1,2}| \leq 0.5$.

2.2. Kilonovae inference

We analyze the AT2017gfo AB magnitudes $d_b(t)$ observed by various telescopes in the photometric bands $b = \{U, B, g, V, R, I, z, J, H, K, K_s\}$ (Villar et al. 2017). The data provide a time coverage of ~ 20 days. These data are provided with their associated standard deviations σ_b , and corrected from reddening effects due to interstellar extinction (Fitzpatrick 1999).

The kN model employed for our analyses is a multi-component semi-analytical template for isotropic homologously-expanding ejecta shells based on (Grossman et al. 2014; Perego et al. 2017b). Nuclear heating rates are described following Korobkin et al. (2012); Barnes et al. (2016). The model includes two ejecta components, each of which is characterized by three parameters: the ejected mass M_{ej} , the root-mean-square velocity v , and the gray opacity κ . From a physical point of view, the less massive and fastest component may be associated to the dynamical ejecta (e.g. Rosswog 2013; Radice et al. 2016), while the slower ejecta component to baryonic winds radiated from the disk (e.g. Perego et al. 2017a; Radice et al. 2018a). Thus, we label the first component as “d” (i.e. dynamical ejecta) and the second as “w” (i.e. baryonic wind). Note, however, that in the inference we do not enforce specific information about the nature of these components, and at the analysis level these just constitute labelling indices used to count the components. We prevent mode switching by ordering the components by decreasing velocity, with “d” the fastest component. The model is implemented and released in *bajes*, which is designed to host more complex semi-analytical models, e.g. Perego et al. (2017a); Ricigliano et al. (2023).

Together with the ejecta parameters, the kN light-curves $\ell_b(t)$ depend also on the extrinsic parameters of the source: the luminosity distance D_L^{kn} , the inclination angle i^{kn} from the polar direction, and the time t_{mrg}^{kn} of coalescence. Moreover, differently from Breschi et al. (2021b), we fix the heating rate parameter $\epsilon_0 = 2 \times 10^{18} \text{ erg g}^{-1} \text{ s}^{-1}$ according to Korobkin et al. (2012). The AB magnitudes are parameterized by 9 degrees of freedom,

$$\theta_{\text{kn}} = \{M_{\text{ej}}^d, v^d, \kappa^d, M_{\text{ej}}^w, v^w, \kappa^w, D_L^{kn}, i^{kn}, t_{\text{mrg}}^{kn}\}. \quad (6)$$

Note that in our analysis, the assumption of isotropic kN removes the dependency on the inclination angle i^{kn} , which in principle can be restored employing anisotropic ejecta profiles Breschi et al. (2021b). However, in the following discussion on joint parameters, we will include this parameter for generality.

We assume that measures performed at different times do not correlate and introduce a Gaussian likelihood for each observed data point (Villar et al. 2017; Perego et al. 2017b; Breschi et al. 2021b). Similarly to Villar et al. (2017), we include an additional correction to the data’s standard deviation. These corrections are inferred during the PE and are useful to mitigate systematic errors of the simple kN model used for the inference. However, differently from Villar et al. (2017), we introduce a correction Σ_b for each photometric band since the kN template can be diversely affected by systematic errors at different electromagnetic

wavelengths. The kN likelihood is

$$\log p(\mathbf{d}_{\text{kn}}|\theta_{\text{kn}}) = -\frac{1}{2} \sum_b \sum_k \frac{[d_b(t_k) - \ell_b(t_k)]^2}{\sigma_b^2(t_k) + \Sigma_b^2} + \log \left[2\pi (\sigma_b^2(t_k) + \Sigma_b^2) \right], \quad (7)$$

where $\ell_b(t)$ represent the kN model described above, k runs over the observed times. Comparing to the GW likelihood, the kN likelihood has a different normalization and it is smaller than one (hence the log-likelihood is negative.) This is not problematic since the posteriors are normalised and the evidence is always relative.

The priors are taken uniform for $M_{\text{ej}}^{(i)} \in [0, 0.5] M_{\odot}$, $v^{(i)} \in [0, 0.333] c$, and $\kappa^{(i)} \in [0, 50] \text{ cm}^2 \text{ g}^{-1}$ for all components, with i running on the components d, w . We do not impose any specific information about the dynamical or wind nature of the component in the prior, Cf. (Breschi et al. 2021b). The prior on the systematic deviations Σ_b is taken as log-uniform constrained to $\log \Sigma_b \leq 5$ magnitudes. This choice corresponds to the Jeffreys (uninformative) prior for standard deviation parameters of normal distributions (see Jaynes 1968).

2.3. Joint & coherent inference

The likelihoods in Eq. (5) and Eq. (7), together with the related prior assumptions, provide a Bayesian framework for the inference of the GW and kN parameters. Within the assumption of different sources (“DS”), the joined prior space is just the space product of the GW and kN parameter spaces,

$$p(\theta_{\text{gw}}, \theta_{\text{kn}}|\text{DS}) = p(\theta_{\text{gw}}) p(\theta_{\text{kn}}), \quad (8)$$

There is no correlation between the GW and the kN parameters in Eq. (8), i.e. $\theta_{\text{gw}} \cap \theta_{\text{kn}} = \emptyset$. However, if the GW and kN transients are (assumed to be) originated from the same source, the spaces in Eq. (9) and Eq. (6) share common parameters. This implies a change of the prior and the sampling, as discussed in the following.

Observations from a single source (“SS”) are related by their extrinsic parameters, i.e. distance $D_L^{\text{GW}} = D_L^{\text{kN}}$, and similarly for the inclination i and merger time t_{mrg} parameters. To impose the above, we introduce the joint set of parameters:

$$\theta_{\text{J}} := \{m_1, m_2, \chi_1, \chi_2, \Lambda_1, \Lambda_2, \psi, \phi_{\text{mrg}}, M_{\text{ej}}^d, v^d, \kappa^d, M_{\text{ej}}^w, v^w, \kappa^w, D_L^J, i^J, t_{\text{mrg}}^J\}. \quad (9)$$

We define the subset of common parameters per given hypothesis as

$$\bar{\theta}_{\text{gw/kn/J}} := \{D_L^{\text{gw/kn/J}}, i^{\text{gw/kn/J}}, t_{\text{mrg}}^{\text{gw/kn/J}}\} \quad (10)$$

Further, by defining:

$$\bar{\bar{\theta}}_{\text{gw}} := \theta_{\text{gw}} / \bar{\theta}_{\text{gw}}, \quad \bar{\bar{\theta}}_{\text{kn}} := \theta_{\text{kn}} / \bar{\theta}_{\text{kn}}, \quad (11)$$

with “/” standing for set subtraction, the set of parameters not shared among the two observations is then:

$$\bar{\bar{\theta}}_{\text{J}} = \bar{\bar{\theta}}_{\text{gw}} \cup \bar{\bar{\theta}}_{\text{kn}}, \quad (12)$$

For concreteness, note that:

$$\bar{\bar{\theta}}_{\text{J}} = \{m_1, m_2, \chi_1, \chi_2, \Lambda_1, \Lambda_2, \psi, \phi_{\text{mrg}}, M_{\text{ej}}^d, v^d, \kappa^d, M_{\text{ej}}^w, v^w, \kappa^w\}. \quad (13)$$

and that:

$$\theta_J = \bar{\theta}_J \cup \bar{\theta}_J \quad (14)$$

The prior distribution on the joint parameters can thus be derived as:

$$p(\theta_J|SS) = \int p(\bar{\theta}_{gw}, \bar{\theta}_{kn}, \bar{\theta}_J, \bar{\theta}_J) d\bar{\theta}_{gw} d\bar{\theta}_{kn}. \quad (15)$$

Since the parameters not shared among the sources are independent of the shared ones, this simplifies to:

$$p(\theta_J|SS) = p(\bar{\theta}_J) \int p(\bar{\theta}_{gw}, \bar{\theta}_{kn}, \bar{\theta}_J) d\bar{\theta}_{gw} d\bar{\theta}_{kn}. \quad (16)$$

Now we can impose the common source hypothesis, which implies:

$$p(\theta_J|SS) = p(\bar{\theta}_J) \int p(\bar{\theta}_{gw}) \delta(\bar{\theta}_{gw} - \bar{\theta}_J) \delta(\bar{\theta}_{kn} - \bar{\theta}_J) d\bar{\theta}_{gw} d\bar{\theta}_{kn}, \quad (17)$$

where $\delta(x)$ is the Dirac distribution. This immediately yields:

$$p(\theta_J|SS) = p(\bar{\theta}_J) p(\bar{\theta}_J). \quad (18)$$

The case discussed enforces a “minimal connection” for a single source, and is weakly dependent on the specific models employed to describe the data. In the following, as $p(\bar{\theta}_J)$ we use a volumetric prior on the inclination ι^J and luminosity distance D_L^J , and a uniform prior on t_{mrg}^J , with boundaries large enough to encompass the full posterior mass. For ease of notation, below we are going to drop the J superscript on the signals parameters.

Further correlation among intrinsic parameters may be introduced assuming a particular source model. For example, NR simulations can provide phenomenological relations between the binary parameters and the mass ejecta properties (e.g. Radice & Dai 2019). The relations considered here specifically relate the dynamical ejecta mass and velocity and the wind’s mass $\theta_{\text{ej}} = \{M_{\text{ej}}^d, v^d, M_{\text{ej}}^w\}$ to the binary masses and the tidal polarizability parameters,

$$\theta_{\text{ej}} \mapsto \theta_{\text{ej}} = F_{\text{NR}}(m_1, m_2, \Lambda_1, \Lambda_2). \quad (19)$$

By assuming Eq. (19), with the same formalism as above, we remove the dependency on θ_{ej} and extend the set of common parameters to $\bar{\theta}_J = \{m_{1,2}, \Lambda_{1,2}, D_L, \iota, t_{\text{mrg}}\}$. Appendix A describes in detail the construction of F_{NR} used in this work. We comment here on two aspects. In brief, first we fit data from a large and heterogeneous set of NR simulations. This provides only a conservative model and a proxy for the current systematic uncertainties on affecting ejecta and kN light curves, e.g. (Radice et al. 2022; Zhu et al. 2020; Barnes et al. 2020; Zappa et al. 2023). For the same reason, we do not consider information on the average electron fraction, that could in principle also be folded into the analysis (Breschi et al. 2021b). Second, NR relations carry errors of the order $\sim 20\%$ that need to be taken into account during PE. Within our Bayesian approach, we account for these uncertainties by including auxiliary recalibration parameters and marginalizing over these additional degrees of freedom (Breschi et al. 2021b, 2022).

Given a prior on the employed parameters, the missing ingredient to define a Bayesian model is the likelihood function. Assuming that the GW and the kN observations are statistically uncorrelated, we write the joint likelihood as the product

$$p(d_{\text{gw}}, d_{\text{kn}} | \theta_{\text{gw}}, \theta_{\text{kn}}) = p(d_{\text{gw}} | \theta_{\text{gw}}) p(d_{\text{kn}} | \theta_{\text{kn}}). \quad (20)$$

Note that the analytical form of Eq. (20) does not depend on the prior choices. While the case discussed here is specific for GW-kN, *bajes* implements a general framework for multimessenger datasets and related analyses.

3. Results

We first perform PE on GW170817 and AT2017gfo when assuming the two signals to have originated from different sources, and then two joint analyses: one assuming a “minimally informed” prior and another using the NR-informed prior. The results of our analyses are summarized in Tab. 1.

3.1. Single messenger analyses

We start by briefly discussing the inference on GW and kN signals, when analysing each dataset separately.

For the GW170817 analyses, we obtain a binary (detector-frame) mass of $M = 2.9^{+0.3}_{-0.2} M_\odot$ and a mass ratio of $q = 1.7^{+0.9}_{-0.6}$, while the measurement of the reduced tidal parameter yields $\tilde{\Lambda} = 160^{+485}_{-146}$. The luminosity distance is constrained to $D_L = 36^{+12}_{-13}$ Mpc. These results are consistent with previous analyses (see, e.g. Abbott et al. 2019b; Breschi et al. 2021a; Tisino et al. 2023). Note that the mass ratio can be sensitive to sampling errors, in particular showing tail extending to large values (Tisino et al. 2023).

For the AT2017gfo analysis, we measure $M_{\text{ej}}^d = 8^{+3}_{-3} \times 10^{-2} M_\odot$ and $v^d = 0.30^{+0.02}_{-0.04} c$, for the mass and velocity of the first component. For the second component, we obtain $M_{\text{ej}}^w = 1.0^{+0.2}_{-0.3} \times 10^{-1} M_\odot$ and $v^w = 4.6^{+0.6}_{-1.4} \times 10^{-2} c$. These ejected masses and velocities are broadly consistent with previous estimates using spherically symmetric models (e.g. Cowperthwaite et al. 2017; Villar et al. 2017; Coughlin et al. 2018; Breschi et al. 2021b). Despite our agnostic prior choice, the PE points towards one component to be less massive and significantly faster with respect to the second component. The inferred ejecta velocities for the lighter (heavier) and faster (slower) components are compatible with the average values predicted by NR simulations for the dynamical and wind ejecta (Nedora et al. 2021a), with the heavier component interpreted as a massive wind emerging from the delayed collapse of the remnant neutron star (Radice et al. 2018b; Nedora et al. 2019; Kiuchi et al. 2022; Radice & Bernuzzi 2023b). However, the inferred dynamical ejecta mass overestimates current NR results by about one order of magnitude. This appears to be a common feature in most of the analyses performed so far, and indicates the need for more sophisticated kN models.

The gray opacities inferred values are more difficult to interpret. On the PE side, this parameter is highly degenerate with distance inclination and total mass, since it controls the signal luminosity. On the modeling side, it is known that the complex atomic and radiation transport physics cannot be adequately captured by a single, averaged and time independent parameter, see e.g. (Ricigliano et al. 2023) for a recent discussion. The luminosity distance is constrained to $D_L = 45^{+5}_{-8}$ Mpc, consistent with GW estimates and measurements of the host galaxy NGC 4993.

In Fig. 3 we show the reconstructed light curves. The employed kN model allows to capture the bulk of the data trend. The quantitative behaviour of the light curve is reproduced over the ~ 20 days period analyzed for several photometric bands. An exception is the pre-peak behaviour in the K -band, which is not accurately reproduced. Further investigations are needed to interpret this feature. Comparing to our previous work (Breschi et al. 2021b), the light curves and opacities were better captured with the parameters and prior choices made there³. We stress that this model is not the best-fitting semi-analytical kN model

³ Note that also a different sampler from Ref. (Pozzo & Veitch ????) was utilized in that work.

Table 1. Median and 90% credible interval of relevant parameters for the different analysis configurations.

		GW170817	AT2017gfo	GW170817+AT2017gfo	GW170817+AT2017gfo (NRI)
M	$[M_\odot]$	$2.9^{+0.3}_{-0.1}$	-	$2.8^{+0.1}_{-0.1}$	$2.77^{+0.03}_{-0.01}$
M_c	$[M_\odot]$	$1.1976^{+0.0005}_{-0.0002}$	-	$1.1976^{+0.0002}_{-0.0001}$	$1.1975^{+0.0001}_{-0.0001}$
q		$1.7^{+0.9}_{-0.6}$	-	$1.4^{+0.3}_{-0.3}$	$1.2^{+0.2}_{-0.2}$
χ_{eff}		$0.05^{+0.08}_{-0.05}$	-	$0.02^{+0.03}_{-0.02}$	$0.00^{+0.01}_{-0.01}$
$\tilde{\Lambda}$		160^{+485}_{-146}	-	684^{+540}_{-382}	667^{+382}_{-270}
$\delta\Lambda$		7^{+118}_{-84}	-	37^{+185}_{-284}	266^{+157}_{-109}
M_{ej}^{d}	$\times 10^{-2} [M_\odot]$	-	8^{+3}_{-3}	$0.1^{+0.1}_{-0.3}$	-
v^{d}	c	-	$0.30^{+0.03}_{-0.06}$	$0.30^{+0.02}_{-0.02}$	-
κ^{d}	$[\text{cm}^2 \text{g}^{-1}]$	-	$0.16^{+0.04}_{-0.02}$	23^{+8}_{-13}	$0.20^{+0.04}_{-0.04}$
M_{ej}^{w}	$\times 10^{-2} [M_\odot]$	-	10^{+3}_{-3}	12^{+3}_{-2}	-
v^{w}	c	-	$0.046^{+0.007}_{-0.015}$	$0.01^{+0.03}_{-0.01}$	$0.03^{+0.01}_{-0.01}$
κ^{w}	$[\text{cm}^2 \text{g}^{-1}]$	-	$0.5^{+0.1}_{-0.2}$	$0.02^{+0.08}_{-0.02}$	$0.4^{+0.2}_{-0.1}$
D_L	$[\text{Mpc}]$	36^{+12}_{-13}	45^{+5}_{-8}	42^{+2}_{-3}	36^{+5}_{-4}
ι	$[\text{rad}]$	$2.4^{+0.5}_{-0.4}$	1.5^{+1}_{-1}	$2.7^{+0.1}_{-0.1}$	$2.4^{+0.2}_{-0.2}$
$\log(L_{\text{max}})$		528.92	-158.22	286.69	366.52

for these analyses, but it is employed here as a first step towards more complex inferences.

3.2. Joint & coherent analyses

We now discuss the impact of the joint analysis on the posterior distribution of the two sets of parameters when performing a joint and coherent analysis.

3.2.1. Agnostic prior on intrinsic parameters

For this analysis, we assumed a common source, but no additional NR-informed priors.

Concerning the GW parameters, a noticeable improvement is observed on the distance (and indirectly on the inclination parameter, as discussed below), now shared among the two models, with a significant tightening of the posterior volume. The chirp mass of the binary remains consistent with the GW-only measurement, with its error bars shrinking. This is not due to direct information on the parameter itself, but is an indirect consequence of the shrinkage in the mass ratio posterior, whose tail is significantly cut by the additional information, pointing towards a comparable-mass system. The improvement in the mass ratio measurement can be in turn traced to the better measurement of the source distance, due to the impact that these parameters share on the GW signal amplitude. The system is now located further away, an effect which can in part be compensated by a higher GW intrinsic luminosity obtained for a more equal-mass system, or by changing the inclination angle. Similarly, the correlation between q and $\tilde{\Lambda}$ implies that larger values of the effective tidal parameter are now favoured. Instead, $\delta\Lambda$ is weakly affected and remains consistent with zero.

Concerning the kN parameters, the velocity of the dynamical component remains essentially unaffected by the joint analysis. The dynamical ejecta mass instead shifts towards much smaller values. This effect is again due to the reduced distance value, which increases the intrinsic source luminosity, hence requiring a lower amount of ejecta to remain consistent with the data. For the wind parameters, the mass remains consistent with the single-source analysis, while the velocity and opacity are pushed towards smaller values, albeit attaining values within the same order of magnitudes with respect to the previous analysis.

3.2.2. NR-informed prior on intrinsic parameters

For this analysis, we instead assumed a common source, and the additional NR-informed prior described above, constraining a subset of the kN intrinsic parameters through binary ones.

Concerning the GW parameters, the chirp mass of the binary keeps remaining consistent with the GW-only measurement, with its error bars slightly shrinking again. This happens for the same reason explained above, as can be appreciated by the overlap between the green posterior in the top left panel of Fig. 1 with the blue posterior. The mass ratio is further shrunked by the NR information, becoming even more consistent with unity, with an impact on $\tilde{\Lambda}$ similar to the one discussed in the case of an agnostic analysis. The inclination remains consistent with the joint analysis performed under the agnostic prior, albeit with a smaller error bar due to a better measurement of the mass ratio, as discussed in the previous case. The NR information also helps in breaking of the degeneracy of the mass ratio with the distance (bottom rightmost panel of Fig. 1). The largest impact from the NR information being imparted on $\delta\Lambda$; while still consistent with the previous measurement, its posterior now prefers non-zero values.

Concerning the kN parameters, the source is now inferred as closer and more off-axis, pushing the wind mass to smaller values. The mass of the dynamical component becomes again consistent with the single-source analysis. The velocities are only mildly affected by the NR-informed prior, with the wind velocity moving away from zero towards values which are again consistent with the kN-only analysis.

3.2.3. Bayes' factors

Within a Bayesian framework, and exploiting the nested sampling algorithm we employed above, it is immediate to compare the evidence for different hypothesis explaining the dataset under consideration, when marginalising over the whole parameter space. Specifically, we are interested in comparing two hypotheses: the “coherent” one, where GW and kN data are simultaneously modelled by a single common source, which we refer to as “SS” following Eq. (17), and the “incoherent” hypothesis, where the two datasets are each explained by independent and disjoint sources, which we refer to as “DS” following Eq. (8).

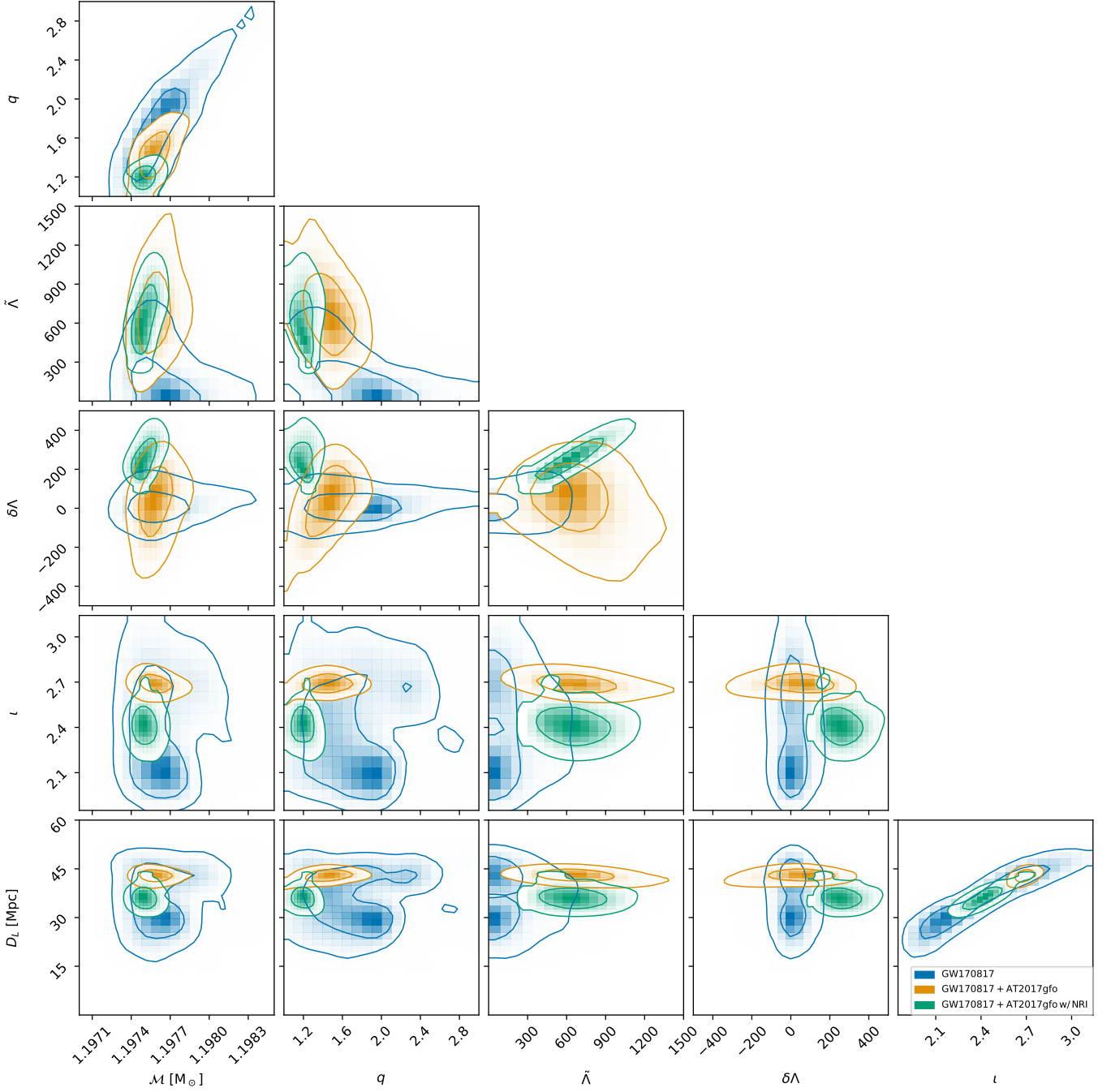


Fig. 1. Posterior distribution for GW relevant parameters under the various assumptions. The contours report the 50% and the 90% credibility regions. Blue posteriors are computed from GW170817 data only, orange (green) posteriors correspond to the joint GW-kN data without (with) NR-informed mappings.

The BF comparing these hypotheses can be obtained through the coherence ratio introduced in Ref. Veitch & Vecchio (2010):

$$\mathcal{B}_{\text{DS}}^{\text{SS}} = \frac{\int d\theta_J p(\theta_J | \text{SS}) p(\mathbf{d}_{\text{gw}} | \theta_J, \text{SS}) p(\mathbf{d}_{\text{kn}} | \theta_J, \text{SS})}{\int d\theta_{\text{gw}} p(\theta_{\text{gw}} | \text{SS}) p(\mathbf{d}_{\text{gw}} | \theta_{\text{gw}}, \text{SS}) \int d\theta_{\text{kn}} p(\theta_{\text{kn}} | \text{DS}) p(\mathbf{d}_{\text{kn}} | \theta_{\text{kn}}, \text{DS})}$$

$$(21) \quad \log_e(\mathcal{B}_{\text{DS}}^{\text{SS-NR}}) = 46.49 \pm 0.2,$$

As discussed in Veitch & Vecchio (2010) in more detail, this ratio intuitively compares the integral of the product with the product of the integrals of the distributions, a measure of how much information is gained by assuming a joint hypothesis. Ad-

ditionally, we label by “SS-NR” the hypothesis obtained when considering the NR-calibrated relation Eq. (19). When applying this computation to the above results, we find:

$$\log_e(\mathcal{B}_{\text{DS}}^{\text{SS}}) = -44.23 \pm 0.2, \quad (22)$$

without assuming NR relations, and:

$$(23) \quad \log_e(\mathcal{B}_{\text{DS}}^{\text{SS-NR}}) = 46.49 \pm 0.2, \quad (23)$$

when assuming NR-calibrated relations.

These results indicate that, within the available dataset and under the employed models, the two observations are better explained by the common source hypothesis (SS) only assuming

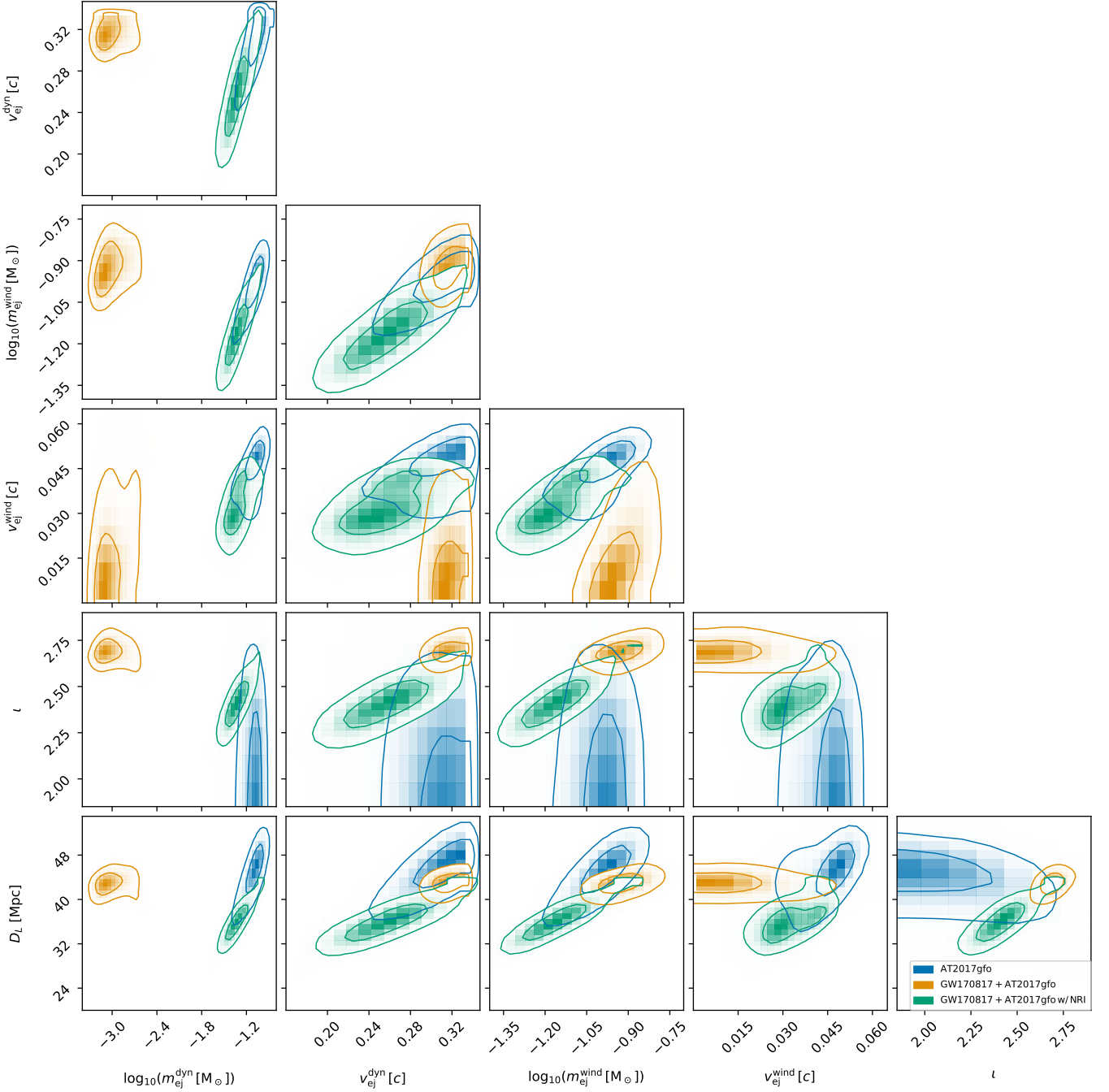


Fig. 2. Posterior distribution for kN relevant parameters under the various assumptions. The contours report the 50% and the 90% credibility regions. Blue posteriors are computed from AT2017gfo data only, orange (green) posteriors correspond to the joint GW-kN data without (with) NR-informed mappings. isotropic model

NR-informed relations. An incoherent explanation (DS) is instead favoured when assuming that only the distance, inclination and coalescence time are assumed to be common parameters. Note that, since the kN model is spherical, the key parameter determining this is the distance, but the latter is compatible among the single messenger analyses. Thus, the negative value of $\log_e(\mathcal{B}_{\text{DS}}^{\text{SS}})$ simply reflects the fact that the distance is consistent in both single messenger analyses and a coherent analysis does not help in fitting the data more than the single messenger analyses. Overall, this result is related to the simplified kN model used in this work and the high degeneracy in kN parameter space discussed above. This underlines the relevance of systematics

in kN modeling, and enforces the importance of informing the models with full numerical solutions by connecting them with binary parameters.

4. EOS constraints

In this section we discuss the constraints on the EOS from our analysis. We follow an approach similar to the one presented in (Breschi et al. 2021b, 2022), with a few key differences. First, we use the updated EOS-insensitive NR relations developed here. Second, we compute a new set of ~ 10 million phenomenological EOS by employing minimal assumptions (Godzieba et al.

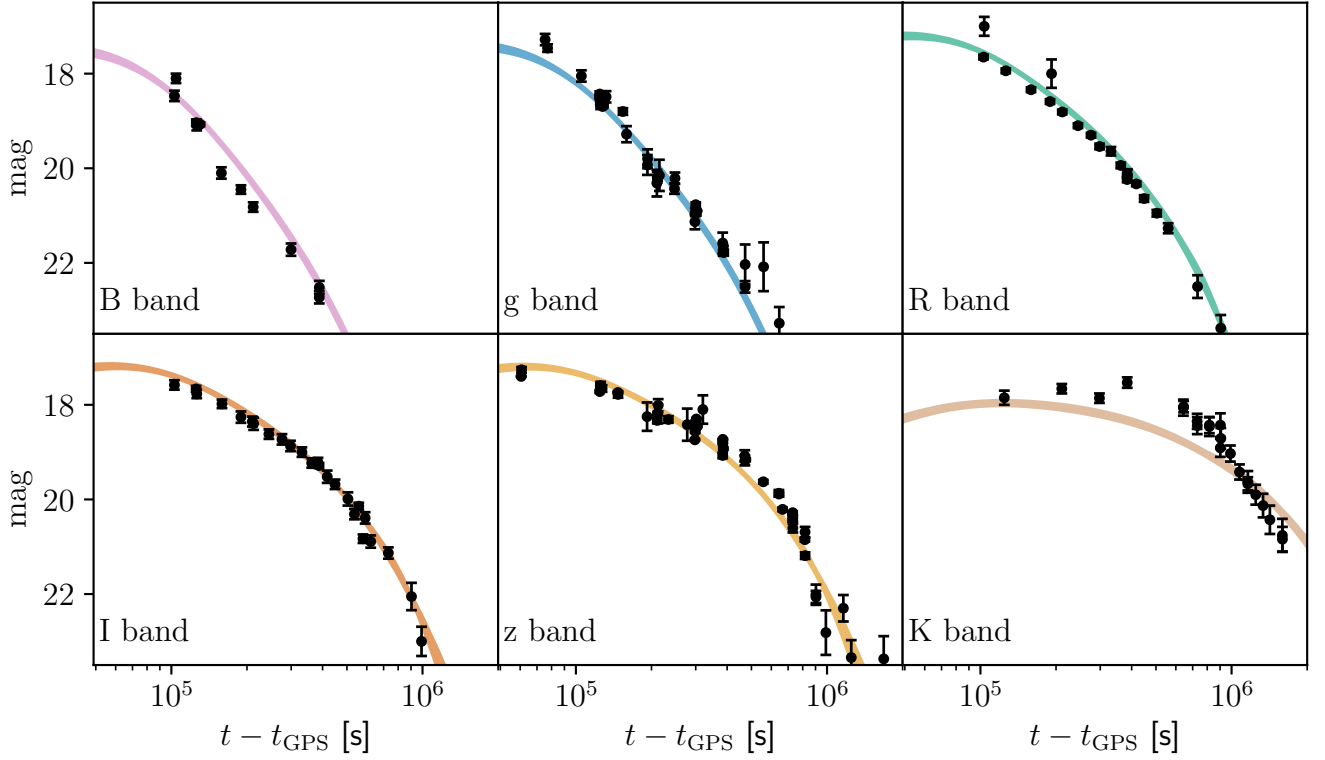


Fig. 3. Light curve reconstruction from the inference on AT2017gfo. The bands represent the parameter variation within their 90% credible regions.

2021). The set is generated with a Markov Chain Monte Carlo approach by fixing the crust EOS and assuming i) general relativity; ii) causality at higher densities. Hence, it is agnostic on nuclear physics and not affected by nuclear physics uncertainties. The set includes EOS with and without first order phase transitions. Differently from (Godzieba et al. 2021), we do not include any constraints from GW170817 and we sample EOS such that $M_{\text{max}}^{\text{TOV}} > 2.09M_{\odot}$ Romani et al. (2022) a posteriori, as described below. Third, we fold-in the pulsars results from Refs. (Miller et al. 2019; Vinciguerra et al. 2023). In order to consistently account for the information listed above we sample over the EOS index in our 10 million set i_{EOS} , as well as over the masses of PSR J0030+0451 (M_{J0030}), PSR J0740+6620 (M_{J0740}) and the masses of the two components of GW170817 progenitor system (m_1, m_2) (Foreman-Mackey et al. 2013). Denoting $\mathbf{d}_{\text{MM}} = \{m_1, m_2, \tilde{\Lambda}\}$, $\mathbf{d}_{\text{J0030}} = \{M_{\text{J0030}}, R_{\text{J0030}}\}$ and $\mathbf{d}_{\text{J0740}} = \{M_{\text{J0740}}, R_{\text{J0740}}\}$, the likelihood we employ is thus given by:

$$p(\mathbf{d}|i_{\text{EOS}}, m_1, m_2, M_{\text{J0030}}, M_{\text{J0740}}) = p_{\text{MM}}(\mathbf{d}_{\text{MM}}|i_{\text{EOS}}, m_1, m_2) \times p_{\text{J0030}}(\mathbf{d}_{\text{J0030}}|i_{\text{EOS}}, M_{\text{J0030}}) \times p_{\text{J0740}}(\mathbf{d}_{\text{J0740}}|i_{\text{EOS}}, M_{\text{J0740}}), \quad (24)$$

where $p_{\text{MM}}(\dots)$, $p_{\text{J0030}}(\dots)$, $p_{\text{J0740}}(\dots)$ are obtained as a gaussian KDE of posteriors from the respective analyses. Similarly, the priors on M_{J0740} , M_{J0030} , m_1, m_2 are obtained from their marginalized one-dimensional posterior, while the prior on the EOS index is assumed to be uniform.

Results are displayed in Fig. 4, and summarized in Tab 2. The addition of kN data to the GW analysis results in a systematic shift of the $R_{1.4}^{\text{TOV}}$ posterior to larger radii of ~ 0.5 km. This is essentially related to the larger $\tilde{\Lambda}$ median and, physically, to the fact that the kN places a lower bound to $\tilde{\Lambda}$ due to disc wind Radice et al. (2018c). The addition of the NR-informed relations to the inference has a relatively small impact on the EOS constraints, with the estimated values of $R_{1.4}^{\text{TOV}}$

and $\Lambda_{1.4}$ compatible within the error bars with the same quantities from the joint analysis. This result is not surprising, as the recovered Λ and M distributions of the two analyses are largely consistent (see Fig. 1). The impact of NICER data on the allowed EOSs, instead, is substantial. The permissibility of certain EOSs (e.g. MS1b) depends on the specific hot-spots model employed (PDT-U or ST+PDT). The estimated distributions of $R_{1.4}^{\text{TOV}}$ are shifted of ~ 1 km between the two models, indicating large systematic errors in the NICER analyses Vinciguerra et al. (2023). Notably, while the evidence of the NICER analysis favors the PDT-U model, the hot spot configuration predicted by the ST+PDT model was found to be more consistent with the gamma-ray emission associated with PSR J0030+0451 (Kalapotharakos et al. 2021).

5. Conclusions

We introduced *bajes-MMA*, a multi-messenger Bayesian pipeline for analyses of signals from binary neutron star mergers. The key features of *bajes* are: (i) The use of NR relations for the ejecta mass and velocities; (ii) The use (and concurrent marginalization) of suitable recalibration parameters, which widen the credible ranges of inferred parameters accounting for systematic uncertainties; (iii) The possibilities of performing joint and coherent analyses. Regarding (ii), this technique is here applied to handle the systematics of phenomenological NR relations used to link remnant properties with the binary properties. More generally, the same methodology could be employed to deal with other types of uncertainties, e.g. in the EOS set. We note that the open source *bajes-MMA* implementation is generic and can accommodate different likelihood, datasets and models.

Our inference results confirm previous findings on the presence of multiple kN components: a faster and lighter “dynamical” component, and a slower and heavier “wind” component.

Table 2. EOS constraints obtained from our multi-messenger PEs. Starting from our agnostic prior set of 10 million EOS, we progressively add the information coming from PSR J0952+0607 ($M_{\text{max}}^{\text{TOV}} > 2.09M_{\odot}$), PSR J0030+0451 and PSR J0740+6620 (NICER), GW170817 (GW) and AT2017gfo (kN). We report the median and 90% credible intervals of the relevant EOS-dependent properties.

Data	$R_{1.4}^{\text{TOV}}$ [km]	$\Lambda_{1.4}$	$M_{\text{max}}^{\text{TOV}}$ [M_{\odot}]	$R_{\text{max}}^{\text{TOV}}$ [km]	$\log_{10} P(2\rho_{\text{sat}})$	$\log_{10} P(4\rho_{\text{sat}})$
Prior	$12.95^{+3.10}_{-1.65}$	540^{+1410}_{-310}	$2.27^{+0.52}_{-0.26}$	$11.90^{+2.80}_{-1.54}$	$34.72^{+0.35}_{-0.29}$	$35.50^{+0.27}_{-0.18}$
$M_{\text{max}}^{\text{TOV}}$	$13.23^{+2.98}_{-1.73}$	620^{+1470}_{-350}	$2.32^{+0.50}_{-0.22}$	$12.15^{+2.72}_{-1.62}$	$34.76^{+0.32}_{-0.29}$	$35.54^{+0.26}_{-0.20}$
$M_{\text{max}}^{\text{TOV}}$ +NICER ^{ST+PDT}	$12.08^{+0.93}_{-0.7}$	360^{+190}_{-110}	$2.25^{+0.26}_{-0.15}$	$11.30^{+1.32}_{-0.82}$	$34.61^{+0.18}_{-0.18}$	$35.53^{+0.14}_{-0.12}$
$M_{\text{max}}^{\text{TOV}}$ +NICER ^{ST+PDT} +GW	$11.86^{+0.95}_{-0.66}$	330^{+180}_{-100}	$2.25^{+0.23}_{-0.14}$	$11.15^{+1.23}_{-0.74}$	$34.56^{+0.18}_{-0.17}$	$35.53^{+0.13}_{-0.10}$
$M_{\text{max}}^{\text{TOV}}$ +NICER ^{ST+PDT} +GW+kN	$12.33^{+0.84}_{-0.81}$	410^{+180}_{-130}	$2.27^{+0.25}_{-0.15}$	$11.48^{+1.30}_{-0.90}$	$34.65^{+0.16}_{-0.17}$	$35.54^{+0.14}_{-0.12}$
$M_{\text{max}}^{\text{TOV}}$ +NICER ^{ST+PDT} +GW+kN (NRI)	$12.30^{+0.81}_{-0.56}$	400^{+180}_{-100}	$2.28^{+0.25}_{-0.16}$	$11.53^{+1.15}_{-0.90}$	$34.64^{+0.16}_{-0.12}$	$35.54^{+0.14}_{-0.12}$
$M_{\text{max}}^{\text{TOV}}$ +NICER ^{PDT-U}	$13.64^{+1.60}_{-1.18}$	740^{+670}_{-300}	$2.35^{+0.40}_{-0.24}$	$12.54^{+1.77}_{-1.45}$	$34.61^{+0.18}_{-0.18}$	$35.53^{+0.14}_{-0.12}$
$M_{\text{max}}^{\text{TOV}}$ +NICER ^{PDT-U} +GW	$12.86^{+0.90}_{-0.83}$	540^{+230}_{-190}	$2.30^{+0.31}_{-0.17}$	$12.08^{+1.54}_{-1.24}$	$34.74^{+0.20}_{-0.15}$	$35.53^{+0.18}_{-0.21}$
$M_{\text{max}}^{\text{TOV}}$ +NICER ^{PDT-U} +GW+kN	$13.30^{+0.87}_{-0.81}$	640^{+280}_{-190}	$2.30^{+0.30}_{-0.20}$	$12.33^{+1.55}_{-1.28}$	$34.77^{+0.20}_{-0.11}$	$35.54^{+0.17}_{-0.22}$
$M_{\text{max}}^{\text{TOV}}$ +NICER ^{PDT-U} +GW+kN (NRI)	$13.20^{+0.91}_{-0.90}$	620^{+270}_{-200}	$2.32^{+0.30}_{-0.19}$	$12.21^{+1.61}_{-1.24}$	$34.76^{+0.21}_{-0.12}$	$35.54^{+0.17}_{-0.22}$

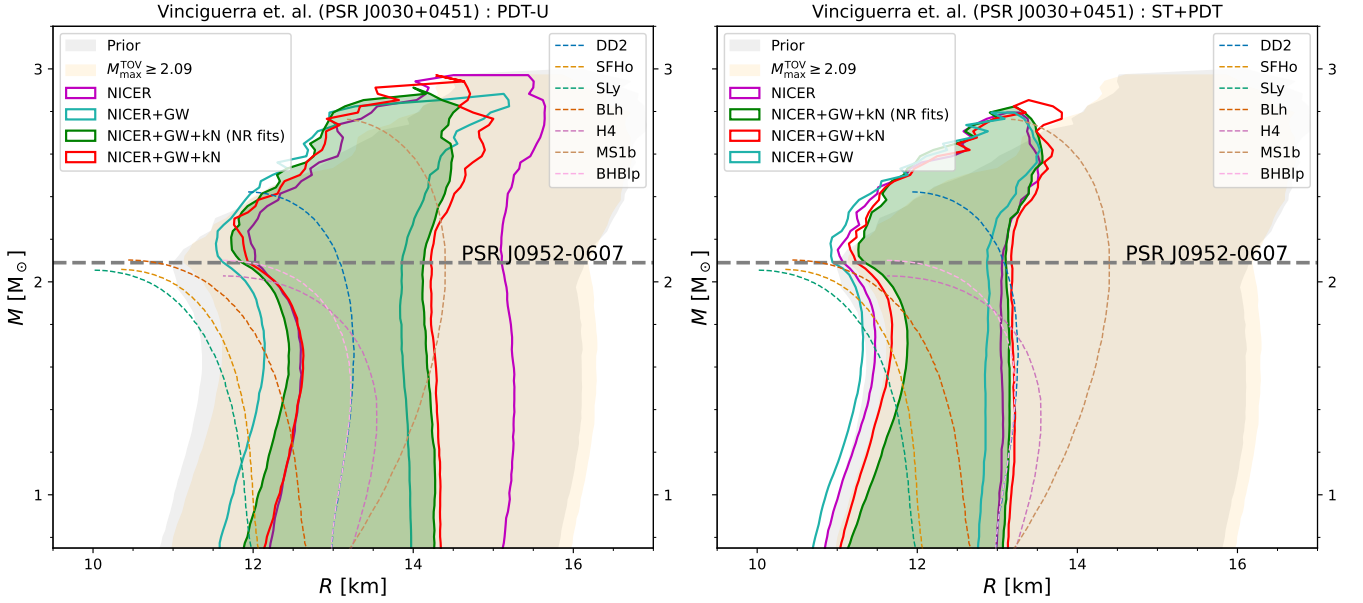


Fig. 4. Constraints on the EOS obtained by resampling the posteriors of the GW-only (blue), joint (red) and NR-informed joint analysis (green) using 10 million EOS and folding in the NICER information of (Vinciguerra et al. 2023), (Miller et al. 2021) and the measurement of $M_{\text{max}}^{\text{TOV}} > 2.09M_{\odot}$ (Romani et al. 2022). Depending on the hot-spot model employed for the analysis of PSR J0030+0451 (PDT-U or ST+PDT, respectively shown in the left and right panels), the EOS constraints shift by ~ 1 km, indicating that (i) NICER data provides strong constraints on the EOS, and (ii) the systematic errors in such analyses are large.

They also indicate consistency in the source distance parameter between GW and kN data. Within spherical kN models, a common GW-kN source is favoured by our joint and coherent analysis only when assuming NR-informed relations between the ejecta components and the binary parameters, capable of significantly breaking the correlations in the GW-kN parameter space. This result also highlights the impact of systematics in kN modeling, and that the degeneracies in kN parameter space can be effectively reduced by incorporating in the inference parametric relations with binary parameters (Raaijmakers et al. 2021b).

Multimessenger analyses with multiple sources can help improving mass-radius diagram constraints. Current observations of GWs and PSRs along with minimal EOS assumptions (validity of general relativity, causality) point to NS maximum masses of $M_{\text{max}}^{\text{TOV}} \sim 2.25 - 2.32$ with errors of $\sim 11\%$ and NS radii $R_{1.4}^{\text{TOV}} \sim 12 - 13$ km with ~ 1 km uncertainty and same order of magnitude systematics. Our results indicate that current gravitational-wave

constraints are compatible with pulsars constraints, in-line with other similar analyses. Pulsars constraints however may be particularly sensitive to systematics, for the data considered this is clearly the case of J0740+6620 (Vinciguerra et al. 2023). Our mass-radius constraints can be translated into constraints into pressure-density constraints for the EOS. For example, at twice saturation densities we find $\log P(2\rho_{\text{sat}}) \approx 34.61 - 34.76$ (depending on systematics), see Tab. 2. Interestingly, such a constraint potentially excludes some of the EOS commonly employed in NR simulations. Future observations of BNSM might improve the precision of these constraints and also help to break systematic effects.

Future work will be devoted to explore more sophisticated kN models as those included in the xkn framework (Ricigliano et al. 2023), as well as kN afterglow models (Hajela et al. 2020; Nedora et al. 2021b). Improved NR relations can be created by utilizing a more homogeneous set of microphysical simula-

tions Nedora et al. (2022) and including the contribution of the disc winds from upcoming long-term simulations Kiuchi et al. (2022); Radice & Bernuzzi (2023a). We also plan to extend the *bajes-MMA* framework to include likelihood and models for GRB and afterglow data, *e.g.* (Biscoveanu et al. 2020; Hayes et al. 2020; Farah et al. 2020; Gianfagna et al. 2023). The inclusion of this messenger can improve the inference of the extrinsic parameters of the source, in particular the viewing angle, with implication for cosmological parameters. However, the inclusion of GRB data in joint analyses is not expected to provide valuable extra information on the EOS because the link between the GRB emission and the NS matter properties is still unclear, *e.g.* (Piran et al. 2013; Hotokezaka et al. 2018) (see also Farah et al. (2020) for similar consideration on the jet structure.)

Acknowledgements. SB acknowledges hospitality and support from the IGC at PSU, where this work was finalized. MB acknowledges support from the European Union’s H2020 under ERC Starting Grant, no. BinGraSp 714626; from the Deutsche Forschungsgemeinschaft (DFG) under Grant no. 406116891 within the Research Training Group (RTG) 2522/1; and from the PRO3 program “DS4Astro” of the Italian Ministry for Universities and Research. RG acknowledges support by the Deutsche Forschungsgemeinschaft (DFG) under Grant No. 406116891 within the Research Training Group RTG 2522/1 and from NSF Grant PHY-2020275 (Network for Neutrinos, Nuclear Astrophysics, and Symmetries (N3AS)) GC acknowledges funding from the Della Riccia Foundation under an Early Career Scientist Fellowship, from the European Union’s Horizon 2020 research and innovation program under the Marie Skłodowska-Curie grant agreement No. 847523 ‘INTERACTIONS’, from the Villum Investigator program supported by VILLUM FONDEN (grant no. 37766) and from the DNRF Chair, by the Danish Research Foundation. SB acknowledges funding from the EU Horizon under ERC Consolidator Grant, no. InspiReM-101043372 and from the Deutsche Forschungsgemeinschaft, DFG, project MEMI number BE 6301/2-1. DR acknowledges funding from the U.S. Department of Energy, Office of Science, Division of Nuclear Physics under Award Number(s) DE-SC0021177, DE-SC0024388, and from the National Science Foundation under Grants No. PHY-2011725, PHY-2116686, and AST-2108467. The computations were performed on the ARA cluster at Friedrich Schiller University Jena, on the supercomputer SuperMUC-NG at the Leibniz- Rechenzentrum (LRZ, www.lrz.de) Munich. ARA, is a resource of Friedrich-Schiller-Universität Jena supported in part by DFG grants INST 275/334-1 FUGG, INST 275/363-1 FUGG and EU H2020 BinGraSp-714626. The authors acknowledge the Gauss Centre for Supercomputing e.V. (www.gauss-centre.eu) for funding this project by providing computing time on the GCS Supercomputer SuperMUC-NG at LRZ (allocations pn36ge and pn36jo).

Appendix A: NR-informed relations for ejecta properties

We derive updated NR-informed EOS-insensitive relations for the dynamical ejecta mass M_{ej}^{d} , the dynamical ejecta velocity v^{d} , and the disk mass m_{disk} . We employ the NR data collected from (Hotokezaka et al. 2013; Bauswein et al. 2013b; Dietrich et al. 2015, 2017; Lehner et al. 2016; Sekiguchi et al. 2016; Radice et al. 2018b; Vincent et al. 2020; Kiuchi et al. 2019; Perego et al. 2019; Endrizzi et al. 2020; Bernuzzi et al. 2020; Nedora et al. 2022), as available for each quantity. The dataset include 262 NR simulations of non-spinning BNS mergers spanning the ranges $M \in [2.4, 4] M_{\odot}$, $q \in [1, 2.05]$ and $\tilde{\Lambda} \in [50, 3200]$. The ejecta data refer to simulations with different degree of physical accuracy (Nedora et al. 2022). Some simulations do not include microphysics and/or neglect neutrino absorption, which are known to be important to describe the mass ejecta, *e.g.* (Perego et al. 2017b). Nonetheless, we employ the entire dataset to provide a conservative constrain within the Bayesian analysis (see below).

The mass of the dynamical component is calibrated using the a factorized empirical analytical form,

$$\log(M_{\text{ej}}^{\text{d}}/M) = a_0 G(\nu) F(m_1, m_2, \Lambda_1, \Lambda_2), \quad (\text{A.1})$$

that includes effects in the symmetric mass ratio $\nu = m_1 m_2 / M^2$,

$$G(\nu) = 1 + g_0 (1 - 4\nu), \quad (\text{A.2})$$

and in the BNS parameters,

$$F(m_1, m_2, \Lambda_1, \Lambda_2) = 1 + b_1 \Lambda_1^{\beta} + c_1 \left(\frac{m_1}{M_{\odot}} \right)^{\gamma} + (1 \leftrightarrow 2). \quad (\text{A.3})$$

The coefficients $\{a_0, b_{1,2}, c_{1,2}\}$ are calibrated on NR data using a differential evolution method. We find the optimal coefficients to be

$$\begin{aligned} a_0 &= -21 \pm 4, & g_0 &= -2 \pm 3, \\ b_1 &= 0.004 \pm 0.001, & c_1 &= -0.5 \pm 0.3, \\ b_2 &= -0.0025 \pm 0.0009, & c_2 &= -0.2 \pm 0.5, \\ \beta &= 1/2, & \gamma &= -1/4, \end{aligned} \quad (\text{A.4})$$

with a $\chi^2 = 4.91$ and a standard deviation of the residuals equal to 13.6%. For the velocity of the dynamical ejecta, we employ a similar fitting formula, where the coefficients are

$$\begin{aligned} a_0 &= 0.09 \pm 0.06, & g_0 &= -5 \pm 2, \\ b_1 &= -0.02 \pm 0.01, & c_1 &= -0.2 \pm 0.9, \\ b_2 &= 0.01 \pm 0.01, & c_2 &= 1.3 \pm 0.6, \\ \beta &= 1/2, & \gamma &= 1, \end{aligned} \quad (\text{A.5})$$

with a $\chi^2 = 12.1$ and a standard deviation of the residuals equal to 21.0%.

We calibrate the disk mass m_{disk} extracted from NR data using the following fitting formula

$$\log\left(\frac{m_{\text{disk}}}{M}\right) = a_0 \chi(\Lambda_1 + \Lambda_2) F(m_1, m_2, \Lambda_1, \Lambda_2), \quad (\text{A.6})$$

where $\chi(\Lambda_1 + \Lambda_2)$ is a correction introduced to for small Λ 's (Radice et al. 2018b),

$$\chi(x) = 1 + \chi_0 \left[\frac{1}{\pi} \arctan\left(\frac{x - \Lambda_0}{\Sigma_0}\right) + \frac{1}{2} \right]. \quad (\text{A.7})$$

The coefficients $\{a_0, b_{1,2}, c_{1,2}, \chi_0, \Lambda_0, \Sigma_0\}$ are calibrated on NR data using a differential evolution method. We find the optimal coefficients to be

$$\begin{aligned} a_0 &= -14 \pm 7, \\ b_1 &= (5 \pm 3) \times 10^{-6}, & c_1 &= -0.5 \pm 0.3, \\ b_2 &= (2 \pm 1) \times 10^{-6}, & c_2 &= 0.3 \pm 0.4, \\ \beta &= 2, & \gamma &= 2, \\ \chi_0 &= -1.00 \pm 0.01, & \Lambda_0 &= 550 \pm 30, & \Sigma_0 &= 180 \pm 30, \end{aligned} \quad (\text{A.8})$$

with a $\chi^2 = 2.64$ and a standard deviation of the residuals equal to 16.4%. As also shown by previous studies (Radice et al. 2018b), the total amount of disk mass increases for increasing tidal polarizability that is consequence of the small compactness of the progenitors, *i.e.* $m/R \simeq 0.1$. We assume that a fraction ξ of the total disk mass contribute to the winds M_{ej}^{w} ,

$$M_{\text{ej}}^{\text{w}} = \xi m_{\text{disk}}^{\text{fit}}. \quad (\text{A.9})$$

None of the relations proposed here is singular on the calibration range, and all formulas are stable in the limit $\Lambda_i \rightarrow 0$.

As discussed above, these NR relations carry non-negligible uncertainties, quantifiable at the $\sim 20\%$ level. In order to marginalize over these theoretical uncertainties, we introduce appropriate calibration parameters δ_k in the PE. These calibration parameters affect the predictions of the dynamical ejecta properties as (Breschi et al. 2021b, 2022)

$$\log(M_{\text{ej}}^{\text{d}}/M) = (1 + \delta_1) \log(M_{\text{ej}}^{\text{d}}/M)^{\text{fit}} \quad (\text{A.10})$$

$$v^{\text{d}} = (1 + \delta_2) (v^{\text{d}})^{\text{fit}}, \quad (\text{A.11})$$

where the superscript “fit” denotes a prediction of an NR-informed relation. The calibration parameters $\delta_{1,2}$ are assumed to be normally distributed with variance prescribed by the residual errors. The disk mass fraction ξ is taken uniformly distributed within the range $[0, 1]$.

Data Availability

bajes is an open-source software available on [GITHUB](#) and on [PyPI](#). For the analyses performed in this work, we employed the newly released version 1.1.0. **TEOBResumS** is publicly developed on [BITBUCKET](#) and available on [PyPI](#).

The GW170817 data are provided by the GWOSC. The AT2017gfo data are collected from Villar et al. (2017). The NICER posteriors are taken from the corresponding references, *i.e.* Miller et al. (2019, 2021); Riley et al. (2019, 2021); Vinciguerra et al. (2023). The EOS prior set is available on the NR-GW open data community on [ZENODO](#). The posterior samples presented in this work will be shared on request to the corresponding author.

References

- Abbott, B. P. et al. 2017a, *Astrophys. J.*, 848, L13
- Abbott, B. P. et al. 2017b, *Phys. Rev. Lett.*, 119, 161101
- Abbott, B. P. et al. 2017c, *Astrophys. J.*, 848, L12
- Abbott, B. P. et al. 2018, *Phys. Rev. Lett.*, 121, 161101
- Abbott, B. P. et al. 2019a, *Phys. Rev.*, X9, 031040
- Abbott, B. P. et al. 2019b, *Phys. Rev.*, X9, 011001
- Abbott, B. P. et al. 2019c, *Phys. Rev. X*, 9, 011001
- Agathos, M., Zappa, F., Bernuzzi, S., et al. 2020, *Phys. Rev.*, D101, 044006
- Akcaay, S., Bernuzzi, S., Messina, F., et al. 2019, *Phys. Rev.*, D99, 044051

- Al-Mamun, M., Steiner, A. W., Näätä, J., et al. 2021, *Phys. Rev. Lett.*, 126, 061101
- Anderson, W. G., Brady, P. R., Creighton, J. D. E., & Flanagan, E. E. 2001, *Phys. Rev. D*, 63, 042003
- Annala, E., Gorda, T., Kurkela, A., Näätä, J., & Vuorinen, A. 2020, *Nature Phys.*, 16, 907
- Antoniadis, J., Freire, P. C., Wex, N., et al. 2013, *Science*, 340, 6131
- Ayriyan, A., Blaschke, D., Grunfeld, A. G., et al. 2021, *Eur. Phys. J. A*, 57, 318
- Barnes, J., Kasen, D., Wu, M.-R., & Martínez-Pinedo, G. 2016, *Astrophys. J.*, 829, 110
- Barnes, J., Zhu, Y., Lund, K., et al. 2020, Preprint (ArXiv:2010.11182) [arXiv:2010.11182]
- Bauswein, A., Baumgarte, T., & Janka, H. T. 2013a, *Phys. Rev. Lett.*, 111, 131101
- Bauswein, A., Goriely, S., & Janka, H.-T. 2013b, *Astrophys. J.*, 773, 78
- Bauswein, A., Just, O., Janka, H.-T., & Stergioulas, N. 2017, *Astrophys. J.*, 850, L34
- Bernuzzi, S., Nagar, A., Dietrich, T., & Damour, T. 2015, *Phys. Rev. Lett.*, 114, 161103
- Bernuzzi, S. et al. 2020, *Mon. Not. Roy. Astron. Soc.* [arXiv:2003.06015]
- Biscoveanu, S., Thrane, E., & Vitale, S. 2020, *Astrophys. J.*, 893, 38
- Brandes, L., Weise, W., & Kaiser, N. 2023, *Phys. Rev. D*, 107, 014011
- Breschi, M., Bernuzzi, S., Godzieba, D., Perego, A., & Radice, D. 2022, *Phys. Rev. Lett.*, 128, 161102
- Breschi, M., Gamba, R., & Bernuzzi, S. 2021a, *Phys. Rev. D*, 104, 042001
- Breschi, M., Perego, A., Bernuzzi, S., et al. 2021b, *Mon. Not. Roy. Astron. Soc.*, 505, 1661
- Capano, C. D., Tews, I., Brown, S. M., et al. 2020, *Nature Astron.*, 4, 625
- Chornock, R. et al. 2017, *Astrophys. J.*, 848, L19
- Coughlin, M. W., Dietrich, T., Margalit, B., & Metzger, B. D. 2019, *Mon. Not. Roy. Astron. Soc.*, 489, L91
- Coughlin, M. W. et al. 2018, *Mon. Not. Roy. Astron. Soc.*, 480, 3871
- Coulter, D. A. et al. 2017, *Science* [arXiv:1710.05452], [Science358,1556(2017)]
- Cowperthwaite, P. S. et al. 2017, *Astrophys. J.*, 848, L17
- Cromartie, H. T. et al. 2019, *Nat. Astron.*, 4, 72
- Damour, T. & Deruelle, N. 1986, *Ann. Inst. Henri Poincaré Phys. Théor.*, 44, 263
- Damour, T. & Nagar, A. 2009, *Phys. Rev.*, D80, 084035
- Damour, T. & Nagar, A. 2010, *Phys. Rev.*, D81, 084016
- Damour, T., Nagar, A., & Villain, L. 2012, *Phys. Rev.*, D85, 123007
- Danielewicz, P., Lacey, R., & Lynch, W. G. 2002, *Science*, 298, 1592
- De, S., Finstad, D., Lattimer, J. M., et al. 2018, *Phys. Rev. Lett.*, 121, 091102, [Erratum: *Phys. Rev. Lett.* 121, no. 25, 259902 (2018)]
- Demorest, P., Pennucci, T., Ransom, S., Roberts, M., & Hessels, J. 2010, *Nature*, 467, 1081
- Dietrich, T., Bernuzzi, S., Ujevic, M., & Brügmann, B. 2015, *Phys. Rev.*, D91, 124041
- Dietrich, T., Coughlin, M. W., Pang, P. T. H., et al. 2020, *Science*, 370, 1450
- Dietrich, T. & Ujevic, M. 2017, *Class. Quant. Grav.*, 34, 105014
- Dietrich, T., Ujevic, M., Tichy, W., Bernuzzi, S., & Brügmann, B. 2017, *Phys. Rev.*, D95, 024029
- Endrizzi, A., Perego, A., Fabbri, F. M., et al. 2020, *Eur. Phys. J. A*, 56, 15
- Essick, R., Tews, I., Landry, P., Reddy, S., & Holz, D. E. 2020, *Phys. Rev. C*, 102, 055803
- Fan, Y.-Z., Han, M.-Z., Jiang, J.-L., Shao, D.-S., & Tang, S.-P. 2023 [arXiv:2309.12644]
- Farah, A., Essick, R., Doctor, Z., Fishbach, M., & Holz, D. E. 2020, *Astrophys. J.*, 895, 108
- Favata, M. 2014, *Phys. Rev. Lett.*, 112, 101101
- Feroz, F., Hobson, M. P., & Bridges, M. 2009, *Mon. Not. Roy. Astron. Soc.*, 398, 1601
- Fitzpatrick, E. L. 1999, *Publ. Astron. Soc. Pac.*, 111, 63
- Foreman-Mackey, D., Hogg, D. W., Lang, D., & Goodman, J. 2013, *Publications of the Astronomical Society of the Pacific*, 125, 306
- Gamba, R., Bernuzzi, S., & Nagar, A. 2021a, *Phys. Rev. D*, 104, 084058
- Gamba, R., Breschi, M., Bernuzzi, S., Agathos, M., & Nagar, A. 2021b, *Phys. Rev. D*, 103, 124015
- Gianfagna, G., Piro, L., Pannarale, F., et al. 2023, *Mon. Not. Roy. Astron. Soc.*, 523, 4771
- Godzieba, D. A., Radice, D., & Bernuzzi, S. 2021, *Astrophys. J.*, 908, 122
- Greif, S. K., Hebeler, K., Lattimer, J. M., Pethick, C. J., & Schwenk, A. 2020, *Astrophys. J.*, 901, 155
- Grossman, D., Korobkin, O., Rosswog, S., & Piran, T. 2014, *Mon. Not. Roy. Astron. Soc.*, 439, 757
- Hajela, A., Margutti, R., Alexander, K. D., et al. 2020, *GRB Coordinates Network*, 29055, 1
- Hayes, F., Heng, I. S., Veitch, J., & Williams, D. 2020, *Astrophys. J.*, 891, 124
- Hebeler, K., Lattimer, J. M., Pethick, C. J., & Schwenk, A. 2013, *Astrophys. J.*, 773, 11
- Hotokezaka, K., Beniamini, P., & Piran, T. 2018, *Int. J. Mod. Phys.*, D27, 1842005
- Hotokezaka, K., Kiuchi, K., Kyutoku, K., et al. 2013, *Phys. Rev.*, D87, 024001
- Hotokezaka, K., Kyutoku, K., Okawa, H., Shibata, M., & Kiuchi, K. 2011, *Phys. Rev.*, D83, 124008
- Huang, C., Raaijmakers, G., Watts, A. L., Tolos, L., & Providência, C. 2023 [arXiv:2303.17518]
- Huth, S. et al. 2022, *Nature*, 606, 276
- Jaynes, E. T. 1968, in *Encyclopedia of Machine Learning*
- Jeffreys, H. 1939, *The Theory of Probability*, Oxford Classic Texts in the Physical Sciences
- Jiang, J.-L., Tang, S.-P., Wang, Y.-Z., Fan, Y.-Z., & Wei, D.-M. 2020, *Astrophys. J.*, 892, 1
- Kalapotharakos, C., Wadiasingh, Z., Harding, A. K., & Kazanas, D. 2021, *Astrophys. J.*, 907, 63
- Kashyap, R. et al. 2022, *Phys. Rev. D*, 105, 103022
- Kiuchi, K., Fujibayashi, S., Hayashi, K., et al. 2022 [arXiv:2211.07637]
- Kiuchi, K., Kyutoku, K., Shibata, M., & Taniguchi, K. 2019, *Astrophys. J.*, 876, L31
- Korobkin, O., Rosswog, S., Arcones, A., & Winteler, C. 2012, *Mon. Not. Roy. Astron. Soc.*, 426, 1940
- Krüger, C. J. & Foucart, F. 2020, *Phys. Rev. D*, 101, 103002
- Le Fèvre, A., Leifels, Y., Reisdorf, W., Aichelin, J., & Hartnack, C. 2016, *Nucl. Phys. A*, 945, 112
- Lehner, L., Liebling, S. L., Palenzuela, C., et al. 2016, *Class. Quant. Grav.*, 33, 184002
- Margalit, B., Jermyn, A. S., Metzger, B. D., Roberts, L. F., & Quataert, E. 2022, *Astrophys. J.*, 939, 51
- Margalit, B. & Metzger, B. D. 2017, *Astrophys. J.*, 850, L19
- Miller, M. C. et al. 2019, *Astrophys. J.*, 887, L24
- Miller, M. C. et al. 2021, *Astrophys. J. Lett.*, 918, L28
- Nagar, A. & Rettegno, P. 2019, *Phys. Rev.*, D99, 021501
- Nagar, A., Riemenschneider, G., Pratten, G., Rettegno, P., & Messina, F. 2020, *Phys. Rev. D*, 102, 024077
- Nagar, A. et al. 2018, *Phys. Rev.*, D98, 104052
- Nedora, V., Bernuzzi, S., Radice, D., et al. 2021a, *Astrophys. J.*, 906, 98
- Nedora, V., Bernuzzi, S., Radice, D., et al. 2019, *Astrophys. J.*, 886, L30
- Nedora, V., Radice, D., Bernuzzi, S., et al. 2021b, preprint (ArXiv:2104.04537) [arXiv:2104.04537]
- Nedora, V., Schianchi, F., Bernuzzi, S., et al. 2022, *Class. Quant. Grav.*, 39, 015008
- Nicholl, M., Margalit, B., Schmidt, P., et al. 2021 [arXiv:2102.02229]
- Nicholl, M. et al. 2017, *Astrophys. J.*, 848, L18
- Pang, P. T. H. et al. 2022 [arXiv:2205.08513]
- Perego, A., Arcones, A., Martin, D., & Yasin, H. 2017a, *JPS Conf. Proc.*, 14, 020810
- Perego, A., Bernuzzi, S., & Radice, D. 2019, *Eur. Phys. J.*, A55, 124
- Perego, A., Logoteta, D., Radice, D., et al. 2022, *Phys. Rev. Lett.*, 129, 032701
- Perego, A., Radice, D., & Bernuzzi, S. 2017b, *Astrophys. J.*, 850, L37
- Pian, E. et al. 2017, *Nature* [arXiv:1710.05858]
- Piran, T., Nakar, E., & Rosswog, S. 2013, *Mon. Not. Roy. Astron. Soc.*, 430, 2121
- Pozzo, W. D. & Veitch, J. ????, <https://github.com/johnveitch/cpnest>, Parallel nested sampling algorithm in python
- Raaijmakers, G., Greif, S. K., Hebeler, K., et al. 2021a, *Astrophys. J. Lett.*, 918, L29
- Raaijmakers, G. et al. 2019, *Astrophys. J. Lett.*, 887, L22
- Raaijmakers, G. et al. 2021b, *Astrophys. J.*, 922, 269
- Radice, D. & Bernuzzi, S. 2023a, *Astrophys. J.*, 959, 46
- Radice, D. & Bernuzzi, S. 2023b, in 15th International Conference on Numerical Modeling of Space Plasma Flows
- Radice, D., Bernuzzi, S., Perego, A., & Haas, R. 2022, *Mon. Not. Roy. Astron. Soc.*, 512, 1499
- Radice, D. & Dai, L. 2019, *Eur. Phys. J.*, A55, 50
- Radice, D., Galeazzi, F., Lippuner, J., et al. 2016, *Mon. Not. Roy. Astron. Soc.*, 460, 3255
- Radice, D., Perego, A., Hotokezaka, K., et al. 2018a, *Astrophys. J. Lett.*, 869, L35
- Radice, D., Perego, A., Hotokezaka, K., et al. 2018b, *Astrophys. J.*, 869, 130
- Radice, D., Perego, A., Zappa, F., & Bernuzzi, S. 2018c, *Astrophys. J.*, 852, L29
- Ricigliano, G., Perego, A., Borhanian, S., et al. 2023 [arXiv:2311.15709]
- Riley, T. E. et al. 2019, *Astrophys. J.*, 887, L21
- Riley, T. E. et al. 2021, *Astrophys. J. Lett.*, 918, L27
- Romani, R. W., Kandel, D., Filippenko, A. V., Brink, T. G., & Zheng, W. 2022, *Astrophys. J. Lett.*, 934, L17
- Rosswog, S. 2013, *Philosophical Transactions A*, 373, 2036
- Russotto, P. et al. 2016, *Phys. Rev. C*, 94, 034608
- Savchenko, V. et al. 2017, *Astrophys. J.*, 848, L15
- Sekiguchi, Y., Kiuchi, K., Kyutoku, K., Shibata, M., & Taniguchi, K. 2016, *Phys. Rev.*, D93, 124046
- Shibata, M., Fujibayashi, S., Hotokezaka, K., et al. 2017, *Phys. Rev.*, D96, 123012

- Skilling, J. 2006, *Bayesian Anal.*, 1, 833
- Smartt, S. J. et al. 2017, *Nature* [[arXiv:1710.05841](#)]
- Speagle, J. S. 2020, *Monthly Notices of the Royal Astronomical Society*, 493, 3132?3158
- Tanaka, M. et al. 2017, *Publ. Astron. Soc. Jap.* [[arXiv:1710.05850](#)]
- Tanvir, N. R. et al. 2017, *Astrophys. J.*, 848, L27
- Tissino, J., Carullo, G., Breschi, M., et al. 2023, *Phys. Rev. D*, 107, 084037
- Valenti, S., Sand, D. J., Yang, S., et al. 2017, *Astrophys. J.*, 848, L24
- Veitch, J. & Vecchio, A. 2010, *Phys.Rev.*, D81, 062003
- Villar, V. A. et al. 2017, *Astrophys. J.*, 851, L21
- Vincent, T., Foucart, F., Duez, M. D., et al. 2020, *Phys. Rev.*, D101, 044053
- Vinciguerra, S. et al. 2023 [[arXiv:2308.09469](#)]
- Vitale, S., Del Pozzo, W., Li, T. G., et al. 2012, *Phys.Rev.*, D85, 064034
- Zappa, F., Bernuzzi, S., Radice, D., & Perego, A. 2023, *Mon. Not. Roy. Astron. Soc.*, 520, 1481
- Zhu, Y., Lund, K., Barnes, J., et al. 2020, preprint ([ArXiv:2010.03668](#)) [[arXiv:2010.03668](#)]